Influence of Ammonia on the Corrosion Behavior of a Zr–Sn–Nb Alloy in High Temperature Water

Zirui Chen*, Yongfu Zhao, Min Tang, Zhaohui Yin, Bin Gong and Zongpei Wu

Reactor Engineering Sub-Institute, Nuclear Power Institute of China, Chengdu, China

Corrosion behaviors, microstructures of oxide films, and hydrogen absorptions of a Chinese domestic Zr alloy in 6.7×10^{-3} mol/L ammonia solution and 2.9×10^{-4} mol/L LiOH+9.3×10^{-2} mol/L H_3BO_3 solution at 360 °C, 18.6 MPa were studied. Weight gains, oxide film thicknesses, and hydrogen absorptions showed that the corrosion rate in the ammonia solution is a little higher than that in the boron–lithium solution. There is no significant difference in the microstructure and crystalline structure between the oxide films formed in the two types of solutions. The element distributions along the depth direction of the oxide films showed the existence of nitrogen in the oxide film formed in ammonia solution. Moreover, nitrogen was found to be segregated in local areas in a range of about 2 µm from the oxide/metal interface. The corrosion behavior of the Chinese domestic Zr alloy in 360 °C aqueous solution shows no difference with other Zr alloys.

Keywords: Zr–Sn–Nb alloy, corrosion rate, ammonia, corrosion behavior, oxide film

INTRODUCTION

Zirconium alloys are the main fuel cladding materials in nuclear power stations (NPPs) as they have low thermal neutron absorption cross section, good corrosion resistance, and mechanical properties (Cox, 2005; Yilmazbayhan et al., 2006; Ni et al., 2012; Motta et al., 2015; Duan et al., 2017). Among the zirconium alloys, Zr–Sn alloys such as zircaloy-2 and zircaloy-4 are widely used in water reactors from the 1950s to the 1990s (Motta et al., 2015). Zr–Nb alloys, such as Zr–2.5Nb and M5 have both good protections against hydrogen ingress and corrosion properties. With the increasing demand for higher burn-up of nuclear fuel, the need for higher waterside corrosion resistance of fuel cladding materials is proposed. Thereupon, Zr–Sn–Nb alloys with better corrosion resistance are developed.

In China, although most of the primary coolant of NPPs is boron–lithium type, there are still several VVER units whose primary coolant is boron–potassium–ammonia type. In the primary coolant, ammonia can not only act as a pH-controlling agent but also can adjust hydrogen concentration by its radiolysis decomposition (Kysela et al., 1996; Kim et al., 2007). However, the corrosion behavior of the Zr alloys especially Zr–Sn–Nb alloy is rarely considered in the boron–potassium–ammonia water chemistry environment. Garzarolli et al. found a large increase in the corrosion rate of zirconium alloy when tested in 20% NH_4OH in 400 °C steam, but only in nickel autoclave (Garzarolli et al., 1993). Titanium, which belongs to the same elemental group as zirconium, also shows acceleration in corrosion and hydrogen absorption when tested in 360°C ammonia aqueous solution (Kim et al., 2002; Kim et al., 2007).

Therefore, it is necessary to study the influence of ammonia on the corrosion behavior of zirconium alloy in 360°C ammonia solution. In this work, the corrosion behavior of a Chinese domestic Zr–Sn–Nb alloy is studied.

TABLE 1 | Chemical composition of the Zr–Sn–Nb alloy (wt%).

Element	Sn	Nb	Fe	O	Zr
Content	0.75–0.95	0.92–1.07	0.23–0.33	0.09–0.13	Bal

TABLE 2 | Aqueous solutions compared in this study.

Type of the solution	Solution compositions	$pH_{300\ °C}$
B-Li (deoxygenated)	2.9×10^{-4} mol/L Li (as LiOH) 9.3×10^{-2} mol/L B (as H_3BO_3)	6.969
NH_4OH (deoxygenated)	6.7×10^{-3} mol/L NH_4^+	6.970
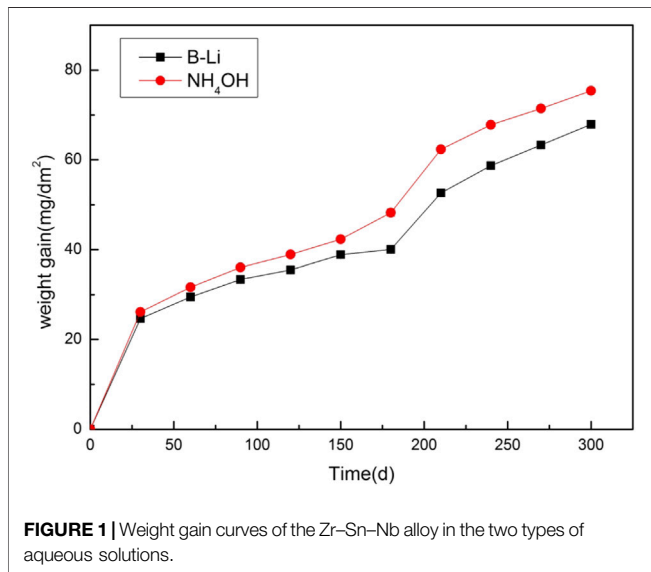
FIGURE 1 | Weight gain curves of the Zr–Sn–Nb alloy in the two types of aqueous solutions.

EXPERIMENTAL

The chemical composition of the Zr–Sn–Nb alloy is listed in **Table 1**. The dimensions of the specimens are 30 mm × 20 mm × 2 mm, and a Φ2-mm hole was drilled on each specimen. All specimens were hung with Zr wires through those Φ2 mm holes during the test. Before the autoclave test, all specimens are grinded by an SiC paper (up to 800#), and pickled in a solution of 10% HF, 45% HNO_3, and 45% H_2O (volume percent) to remove surface oxide formed during manufacturing. In order to show the influence of ammonia, two types of aqueous solutions with close $pH_{300\ °C}$ were compared as shown in **Table.2**. The B–Li solution is a common simulated primary loop coolant in pressurized water reactor NPPs. The autoclave tests lasted for 300 days at 360℃ and 18.6 MPa. The weight gain of all specimens was measured every 30 days during the whole test. In general, the corrosion test followed the ASTM G2/G2M-19 Standard.

The crystalline structures of the oxide films were analyzed using Bruker D8 Discovery X-ray diffraction (XRD) in the scanning range of 10–80° (2θ). A JSM-7500F field emission

scanning electron microscope (FESEM) attached with an energy dispersive spectroscopy (EDS) was used to observe the surface, the cross-sectional morphology of oxidation films, and chemical compositions of the specimens. Thin foils of cross sections of the oxide films were prepared using a Helios Nanolab 600i focused ion beam (FIB) with an initial milling current of 7,000–300 pA at 30kV. The morphologies and microstructures of the cross section of oxide films were observed by an FEI Themis Z transmission electron microscope. The distributions of elements in oxide films along the depth direction were measured by performing glow discharge optical emission spectrometry (GDOES) analyses. The hydrogen contents of the corroded specimens were analyzed by using a HORIBA EMGA-800 oxygen/nitrogen/hydrogen determinator, and the hydrides were observed in the cross sections of the matrix of the corroded specimens using an optical microscope.

RESULTS

Figure 1 shows the weight gain curves of the Zr–Sn–Nb alloy in the two types of aqueous solutions for 300 days. The fitted weight gain–corrosion time relationships are listed in **Table 3**.

As shown in **Figure 1**, the corrosion behavior of the Zr–Sn–Nb alloy in two types of aqueous solutions seems to follow the same law. Both transitions occur after about 180 days. The oxidation kinetics follow a parabolic trend during post-transition, as fitted in **Table 3**. The corrosion rate of the Zr–Sn–Nb alloy in the B–Li solution is a little lower than that in the NH_4OH solution. After the 300-day tests, the weight gains of the Zr–Sn–Nb alloy in B–Li solution and in NH_4OH solution are about 67.15 mg/dm² and 75.44 mg/dm², respectively.

Figure 2 shows the surface morphologies of the oxidation films on the specimens after 30, 90, 150, 240, and 300 days of tests in the two types of solutions. After first 30 days of test, compact oxide films can already be seen on the specimens in both two types of solutions. Wave terrains which may be related to inhomogeneous oxidation can be found on all specimens. No cracks but a few microspores and oxide particles were found on the surfaces of the specimens. No apparent changes in the oxidation morphology were found as the tests went on. The EDS results show that the chemical compositions of all specimens after different days of test in the two types of solutions were nearly the same as shown in **Table 4**. All of them are oxides with about 70 wt% Zr.

The cross-sectional morphologies of the oxide films on the specimens after 30, 90, 150, 240, and 300 days of test in the two types of solutions are shown in **Figure 3** (the white dotted lines in the images are the oxide/metal interface marked by the authors). The cross-sectional morphologies show that the oxide films are compact and uniform in thickness. Preferential oxidation can be found in some local areas. In the oxide films on specimens tested in NH_4OH solution, a few short cracks which are parallel to the surface can be found after 150 days of the test. In the specimens tested in B–Li solution, a few cracks can also be found in oxide files near oxide/metal interfaces. These cracks are usually formed due to inhomogeneous oxidation in local areas which leads to

TABLE 3 | Fitted weight gain–corrosion time relationships of the Zr–Sn–Nb alloys.

Type of the solution	Pre-transition (T = 30–180 days)	Post-transition (T = 180–300 days)
Li–B	$\Delta M' = 0.1021T + 22.933$	$\Delta M' = 2.5164 (T-180)0.5 + 39.5806$
NH_4OH	$\Delta M' = 0.1383T + 22.708$	$\Delta M' = 2.4636 (T-180)0.5 + 48.4519$
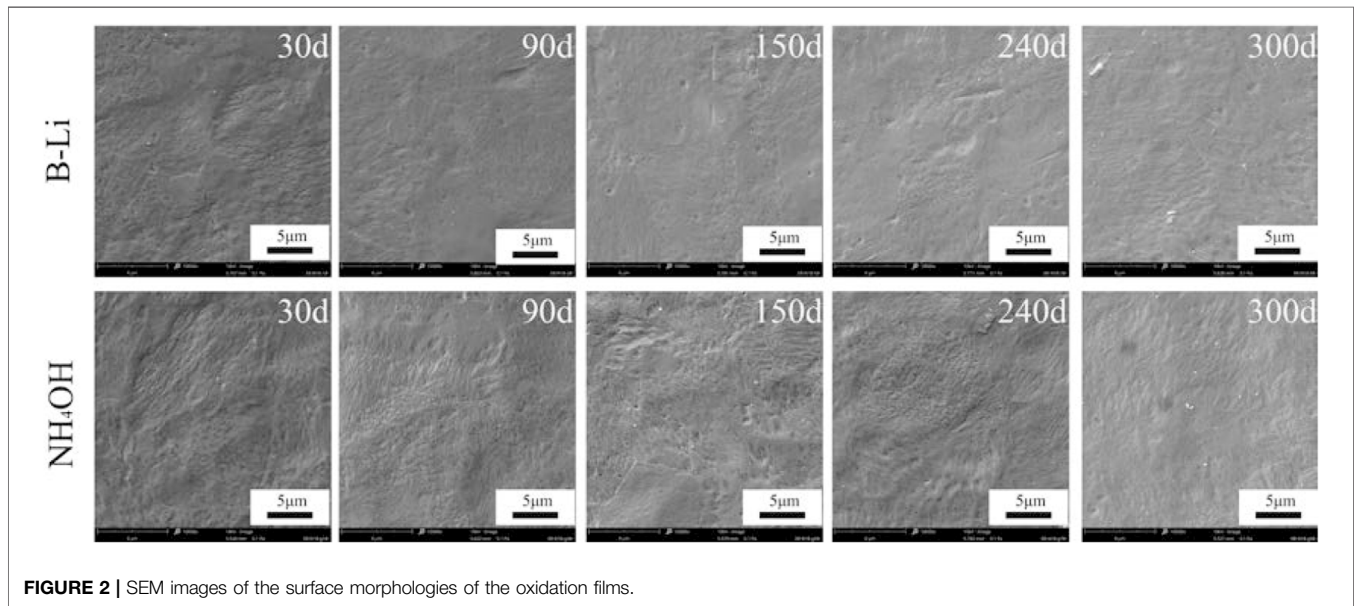
FIGURE 2 | SEM images of the surface morphologies of the oxidation films.

TABLE 4 | EDS results of the chemical compositions of the surface oxide films (wt%).

Type of the solution	Element	30d	90d	150d	240d	300d
B–Li	Zr	71.39	70.84	73.46	70.99	69.50
	O	24.26	25.06	25.61	24.98	25.60
	Nb	3.74	3.33	0.00	3.42	3.87
	Fe	0.47	0.57	0.48	0.62	0.68
	Cr	--	0.20	0.16	--	0.06
	Sn	0.14	--	--	--	--
NH_4OH	Zr	71.69	71.69	68.41	71.37	71.06
	O	24.80	24.60	27.91	24.48	24.88
	Nb	3.41	3.71	3.58	3.56	3.61
	Fe	0.10	--	0.10	0.46	0.33
	Cr	--	--	--	0.13	--
	Sn	--	--	--	--	--

tensile stress perpendicular to the surface and compressive stress parallel to the surface (Polatidis et al., 2013). As the cracks appeared earlier in the specimens tested in NH_4OH solution than those tested in B–Li solution, it can be concluded that the corrosion rate of the specimens tested in NH_4OH solution is faster.

The thickness of the oxide films is the average value of ten sites which were randomly selected on each specimen. The results are shown in **Figure 4**. The oxide films on the specimens tested in the NH_4OH solution are a little thicker than those tested in the B–Li

solution. It is consistent with the weight gain results shown in **Figure 1**. Moreover, the error bars shown in **Figure 4** also reveal the inhomogeneous oxidation of the Zr–Sn–Nb alloy, which is commonly found in Zr alloys (Liu et al., 2019).

Figure 5 shows the XRD results of the specimens tested in the two types of solutions after 30, 150, and 300 days. After 30 days of the test, most of the strong diffraction peaks are Zr matrix and a few of them are tetragonal-ZrO_2 (t-ZrO_2) on the specimens tested in both types of solutions. This is because the oxide films are rather thin and the X-ray diffraction results show information of Zr-matrix under the oxide films. The other reason is that there may still be some unoxidized Zr-matrix among the oxide films. After 150 days of the test, a lot of weak monoclinic-ZrO_2 (m-ZrO_2) peaks appeared, which means that lots of m-ZrO_2 oxides nucleated. But strong peaks show that there are still a lot of t-ZrO_2 and Zr matrices on the surface. It is consistent with the results of Kritskii et al. (Kritskii et al., 2013). After 300 days of the test, strong m-ZrO_2 peaks can be found in both XRD spectrums. Moreover, the m-ZrO_2 peaks from the surface of the specimens tested in NH_4OH solution are even stronger, which means that there may be more m-ZrO_2 on the specimens tested in solution than those tested in B–Li solution (Gravie and Nicholson, 1972; Garzarolli et al., 1991; Gravie and Nicholson, 2006). The oxidation process of Zr is often as follows: t-ZrO_2 first formed, and as the process went on, t-ZrO_2 transformed into m-ZrO_2 (Malinovschi et al., 2017; Balakrishnan et al., 2018); it can be concluded that the t-ZrO_2 to m-ZrO_2 transformation is faster in the specimen tested in NH_4OH solution.
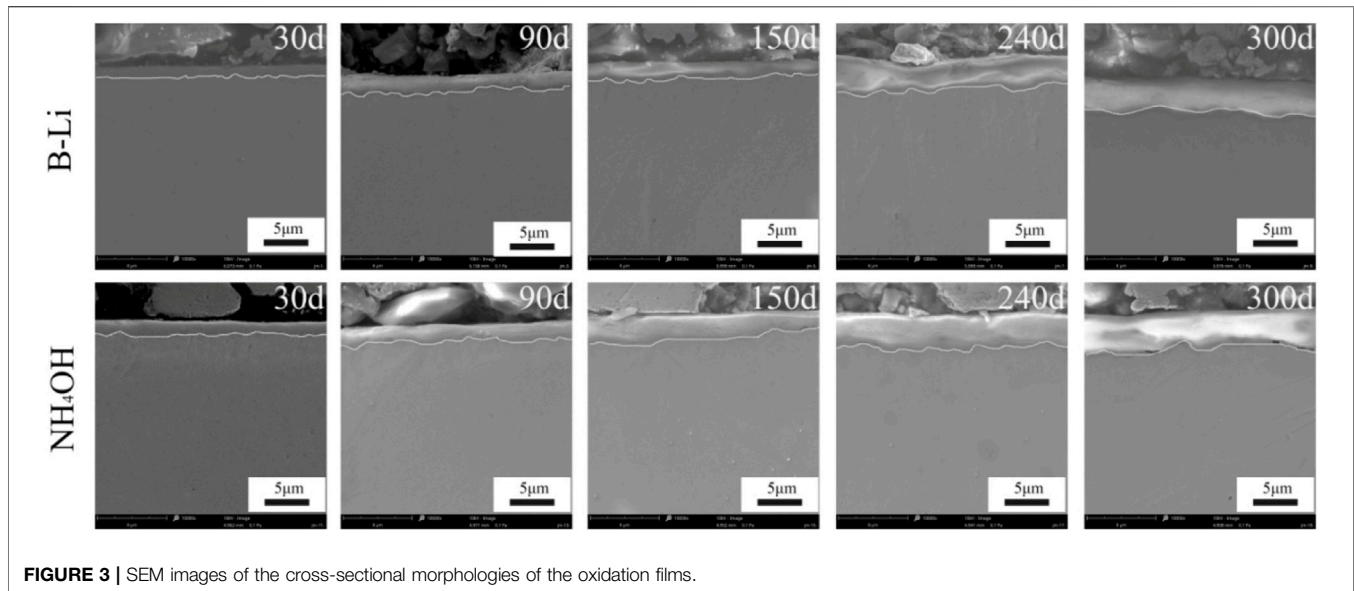
FIGURE 3 | SEM images of the cross-sectional morphologies of the oxidation films.
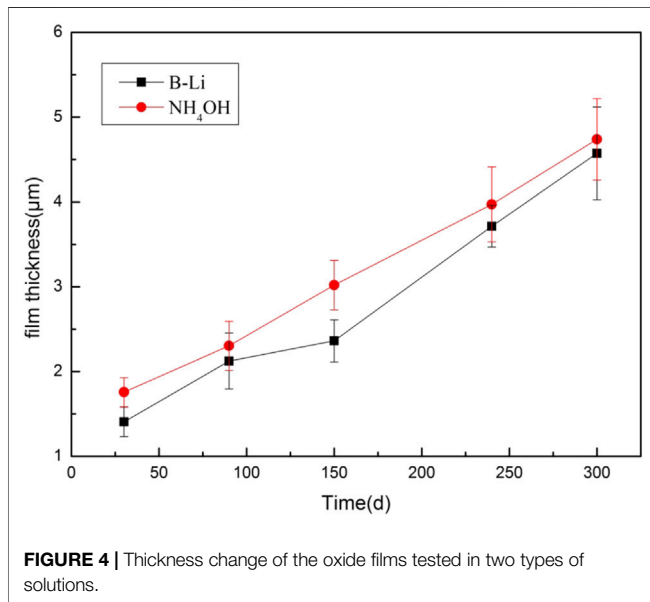

FIGURE 4 | Thickness change of the oxide films tested in two types of solutions.

Figures 6A,C show the cross-sectional morphologies of oxide films on the specimen tested in B–Li solution and NH_4OH solution after 300 days, respectively. It can be found that both the two oxide films are formed by a layer of equiaxed crystal with a thickness of 300–500 nm and a columnar crystal layer beneath it. **Figures 6B,D** are the high-resolution TEM (HRTEM) images taken from the equiaxed layers of **Figures 6A,C**, respectively. It is obvious that the grain size of both the equiaxed crystals ranges from 5 to 30 nm. Fast Fourier transformations (FFT) were carried out according to the images marked by white squares in **Figures 6B,D**. The results show that these equiaxed crystals are m-ZrO_2 oxides which are consistent with XRD results. In general, there is no difference in oxide morphology, crystalline structure, and

grain size between the oxide films on the specimens after 300 days of the test in both B–Li and NH_4OH solutions.

Figure 7 shows the hydrides precipitated in the matrix of the specimens after 30, 90, 150, 240, and 300 days of the test in the two types of solutions. Vermicular hydrides can be found randomly distributed in the matrix. The lengths of the hydrides increase with the experiment going on in both types of solutions. In the first 90 days of the experiment, the lengths of the hydrides are almost the same. After 150 days of the experiment, the hydrides in the specimens tested in NH_4OH solution are much longer than those tested in B–Li solution. Especially in the specimens after 300 days tested in NH_4OH solution, some of the hydrides seem interconnected.

An oxygen/nitrogen/hydrogen determinator was used to measure the hydrogen absorption concentration in the specimens after the experiment, and the results are shown in **Table.5**. The hydrogen absorption concentrations in the specimens tested in both the two solutions increase as the experiments go on. After 150 days of the test, the hydrogen absorption concentration in specimens tested in NH_4OH solution is relatively higher than that tested in B–Li solution.

The distributions of B, Li, N, H, and O in oxide films along the depth direction on the specimens after 300 days test are shown in **Figure 8**. Taking elements' diffusion into account, the middle points in the last segments of oxygen content trend curves are considered oxide/metal interfaces as marked in **Figure 8**. The thicknesses of the oxide films got through this method are very close to the results shown in **Figure 4**. It also can be found that the oxide film formed in NH_4OH solution is a little thicker than that formed in B–Li solution which is consistent with **Figure 4**. It is apparent that nitrogen existed in the oxide film formed in the NH_4OH solution, while there is no nitrogen in the oxide film formed in the B–Li solution. In the range where the depth is from 2 to 4μm, local enrichment of nitrogen can be found. In the matrix near the oxide/metal interface, a very small amount of nitrogen can also be found.
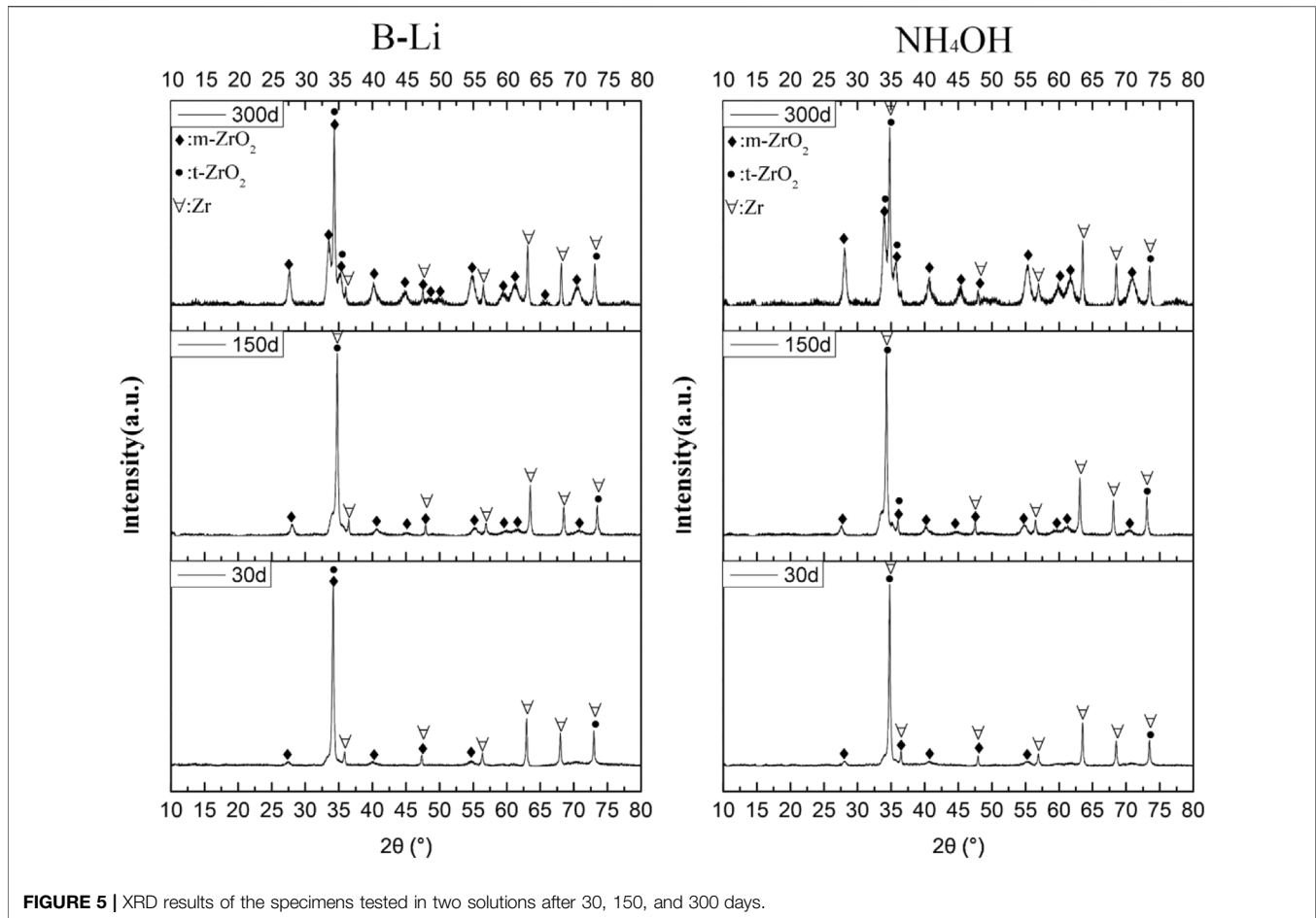
FIGURE 5 | XRD results of the specimens tested in two solutions after 30, 150, and 300 days.

DISCUSSION

The weight gain of the Zr–Sn–Nb alloy tested in NH₄OH solution is higher than that tested in B–Li solution throughout the whole 300 days of the experiment. It is consistent with the results of the thickness of the film, lengths of hydrides in the matrix, and hydrogen absorption. As the pH of the NH₄OH solution is quite close to the pH of the B–Li solution at a high temperature, it can be inferred that the addition of ammonia leads to an increase in weight gain. Moreover, the XRD and TEM results showed that there were no differences in the morphologies, phases, and crystalline structures of the oxides on the specimens tested in the two types of solutions. It means that the addition of ammonia only increases the corrosion rate of the Zr–Sn–Nb alloy to some extent, but did not change the corrosion mechanism. In general, the corrosion behavior of the Zr–Sn–Nb alloy in 360˚C aqueous solution shows no apparent difference with other Zr alloys (Han and Rheem, 1994; Dong et al., 2013; Lai et al., 2020).

However, the GDOES results showed the existence of nitrogen in the oxide film on the specimen tested in the NH₄OH solution. As former studies show that when the concentration of nitrogen in the Zr alloy exceeds 0.004%, the corrosion rate will significantly increase (Lustman and Kerze, 1955). In this study, the nitrogen concentration of the oxide/metal interface is much higher than 0.004%, as shown in **Figure 8**.

The influence of traces of nitrogen on the corrosion rate of the Zr alloy can be explained as follows (Macdonald, 2012; Motta et al., 2015): oxygen in the water molecule first dissociates and is absorbed onto the oxide film surface. Then the oxygen ions move in the oxide film through oxygen vacancies of the oxide film and finally reach the oxide/metal interface. When they reach the oxide/metal interface, they react with zirconium cations to form new oxide. Meanwhile, electrons in the metal matrix move from the metal surface toward the oxide film, and finally, they were taken away by an oxidizing agent in the environment. The control mechanism of the corrosion rate is the movement velocity of oxygen, oxygen vacancies, and electrons. Therefore, the oxygen vacancy amount is one of the key factors that affect the corrosion rate of Zr alloys. In the ZrO_2 oxide film, the chemical valences of oxygen ion, oxygen vacancy, and Zr are -2, +2, and +4, respectively. As interstitial cations in the environment move into the ZrO_2 film, oxygen vacancy amount will decrease to maintain electric neutrality (Krausová et al., 2015; Wei et al., 2020a). However, when substantial cations whose chemical valence is lower than +4 or anions whose chemical valence is higher than -2 (-3, -4, *etc.*)
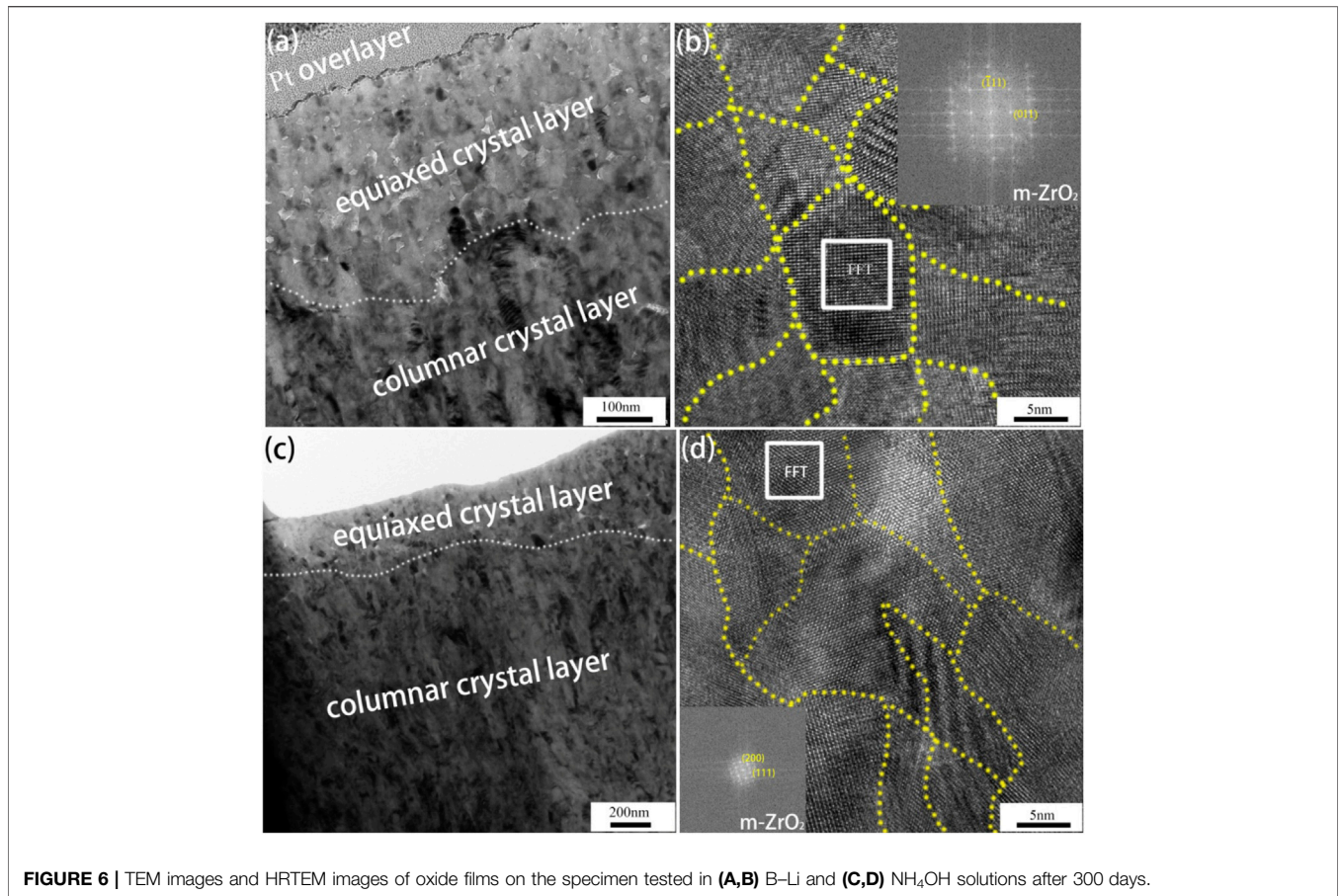
FIGURE 6 | TEM images and HRTEM images of oxide films on the specimen tested in **(A,B)** B–Li and **(C,D)** NH₄OH solutions after 300 days.
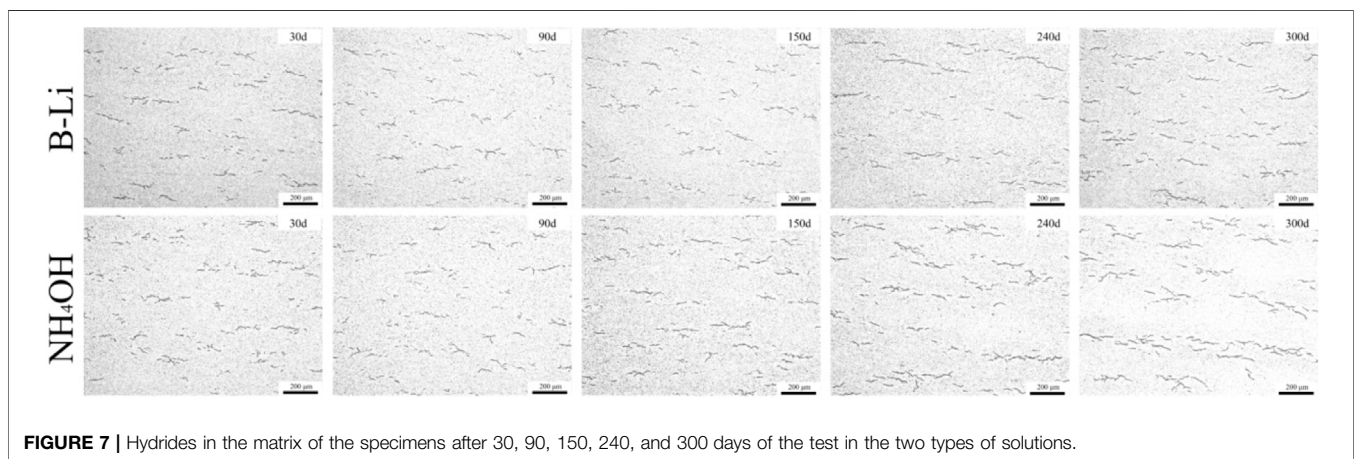

FIGURE 7 | Hydrides in the matrix of the specimens after 30, 90, 150, 240, and 300 days of the test in the two types of solutions.

move into the ZrO_2 oxide film, oxygen vacancies amount will increase. N^{3-} can easily substitute O^{2-} in the ZrO_2 film as their radiuses are very close (N^{3-} 146p m and O^{2-} is 132p m); therefore, the corrosion rate of Zr will increase when N^{3-} moves into the ZrO_2 oxide film.

The corrosion process of the Zr alloy briefly contains the following reactions:

1. The Zr atoms in the Zr alloy matrix lose electrons and become Zr cations at the oxide/metal interface. The electrons move toward the oxide/solution interface, that is, $Zr \rightarrow Zr^{4+} + 4e^-$.
2. The Zr cations react with free oxygen to form ZrO_2 oxides at the oxide/metal interface which leads to oxide front advance into metal. In the meantime, oxygen vacancies form, that is, $Zr^{4+} + 2O \rightarrow ZrO_2 + 2V_o^{2+}$ (V_o oxygen vacancy).
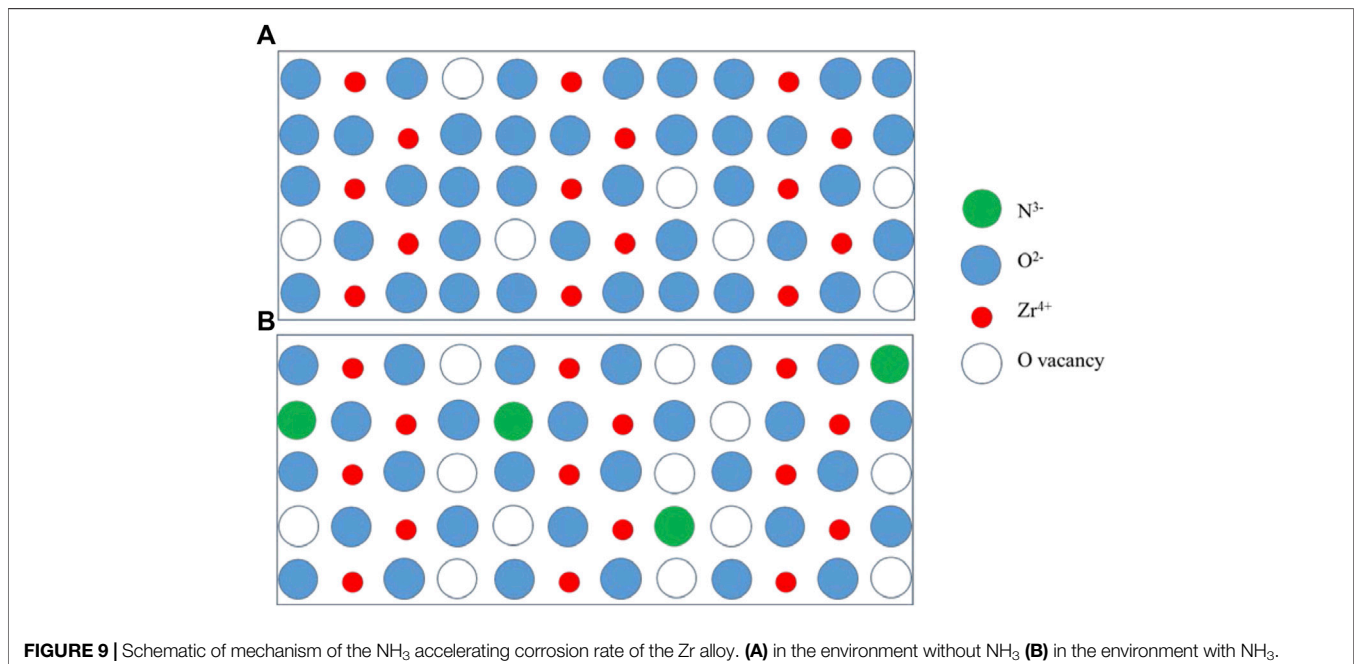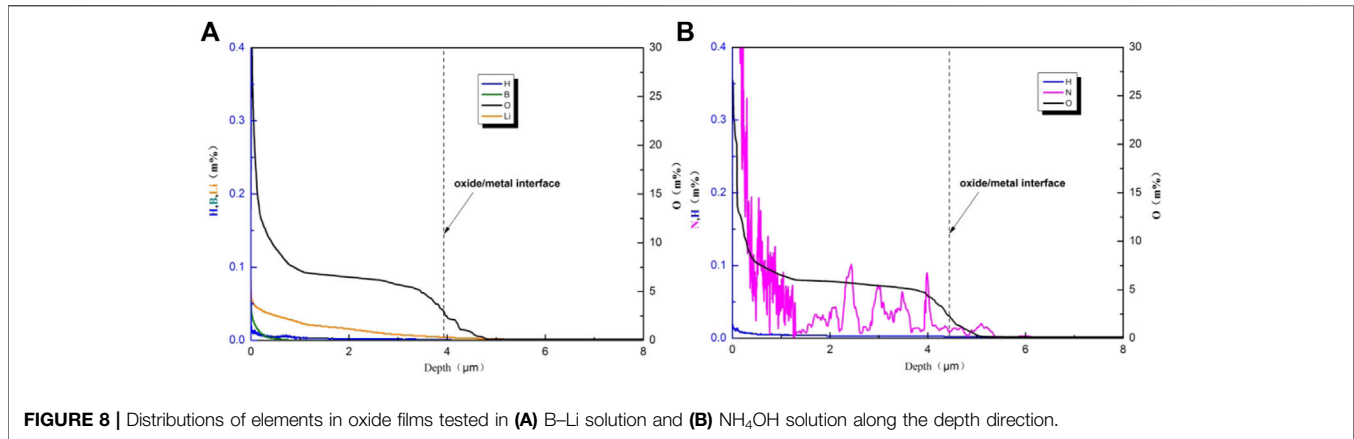
TABLE 5 | Hydrogen absorption in the specimens in the two solutions after 30, 150, and 300 days of the test.

Type of aqueous solution	30d	150d	300d
Li–B–NH$_4$OH	20	19	36
NH$_4$OH	19	29	59

3. The oxygen vacancies move to the oxide/solution interface and capture oxygen ions in the environment, and then oxygen atoms move toward the oxide/metal interface, that is, $V_o^{2+} + O^{2-} \rightarrow O$.

4. A total of four protons at the oxide/solution interface get electrons in the oxides and are reduced into hydrogen, that is $2H^+ + 2e^- \rightarrow H_2$.

It must be mentioned that the reactions above only generalize a simplified corrosion process. The actual corrosion process that may contain other reactions is more complicated.

The mechanism of NH$_3$ accelerating the corrosion rate of the Zr alloy is shown in **Figure 9**. In an environment without NH$_3$, the schematic of the ZrO$_2$ lattice which contains Zr^{4+}, O^{2-}, and oxygen vacancies is shown in **Figure 9A**. The number ratio of Zr^{4+} to O^{2-} is 1:2 in a perfect ZrO$_2$. Considering the existence of a few O vacancies, the number ratio will be a little lower than 1:2. When NH$_4$OH is present in the environment, N^{3-} can easily occupy O vacancy in the ZrO$_2$ lattice by the third reaction mentioned above. As N^{3-} has one more negative charge than O^{2-}, one oxygen vacancy will form to maintain electrical neutrality when two N^{3-} get into the ZrO$_2$ lattice, as shown in **Figure 9B**. Therefore, the more N^{3-} gets into the ZrO$_2$ lattice, the more O^{2-} vacancies form, and the corrosion rate increases.

FIGURE 8 | Distributions of elements in oxide films tested in **(A)** B–Li solution and **(B)** NH$_4$OH solution along the depth direction.

FIGURE 9 | Schematic of mechanism of the NH$_3$ accelerating corrosion rate of the Zr alloy. **(A)** in the environment without NH$_3$ **(B)** in the environment with NH$_3$.

One interesting result is that boron and lithium were also found in the oxide film on specimens tested in the B–Li solution as shown in **Figure 8**. According to the discussion above, the presence of Li^+ and B^{3+} in the ZrO_2 film will also increase the corrosion rate if they act as substantial ions. Actually high concentration of Li^+ will significantly increase the corrosion rate of the Zr alloy as the ion radiuses of Li^+ and Zr^{4+} are very close (Li^+ is 76p m and Zr^{4+} is 72p m) (Cox and Wu, 1995; Wei et al., 2020b). It was found that lithium will segregate at grain boundaries of ZrO_2 (Xie et al., 2020). However, lithium concentration in B–Li solution in this study is only 2.9×10^{-4} mol/L (2ppm), which is too low to result in acceleration of corrosion. For boron, maybe it is too difficult to substitute Zr^{4+} as its ion radius is only 23p m. In **Figure 8A**, it is found that the boron concentration is very low to cause an effect.

CONCLUSION

The corrosion behaviors of a Chinese domestic Zr–Sn–Nb alloy in ammonia solution and boron–lithium solution at 360 °C, 18.6 MPa are studied in this work. The weight gains, oxide morphologies, crystalline structures of oxide, hydrogen absorptions, hydride morphologies, and element distributions of oxide are compared. The conclusions are as follows:

1. There is no difference in microstructures and crystalline structures between oxide films formed in 6.7×10^{-3} mol/L ammonia solution and 2.9×10^{-4} mol/L LiOH+9.3×10^{-2} mol/L H_3BO_3 solution after exposure for 300 days at 360°C, 18.6 MPa. The microstructures of both oxides consist of an equiaxed crystal layer with a thickness of 300–500 nm and a columnar crystal layer beneath it. The crystalline structures of both oxides consist of most monoclinic-ZrO_2 and a few tetragonal-ZrO_2.

2. The corrosion behavior of the Zr–Sn–Nb alloy in 360 °C aqueous solution shows no difference with other Zr alloys.

3. Based on the results of weight gains, oxide thickness, and hydrogen absorptions, the presence of ammonia will not significantly change the corrosion rate of the Zr–Sn–Nb alloy, but only cause a little bit increase in the corrosion rate. During pre-transition, the weight gain of the Zr–Sn–Nb alloy in the B–Li solution is only about 2 mg/dm^2 than that in the NH_4OH solution. During post-transition, the weight gain in the B–Li solution is about 8 mg/dm^2 than that in the NH_4OH solution.

4. Nitrogen in ammonia can move into ZrO_2 oxide and segregate at local areas in a range of about 2 μm from the oxide/metal interface, which may be the reason for the acceleration of the corrosion rate.

DATA AVAILABILITY STATEMENT

The datasets presented in this article are not readily available because they are currently under embargo, while the research findings are commercialized. Requests for data 12 months after publication of this article will be considered by the corresponding author. Requests to access the datasets should be directed to Chen Zirui, raymix@aliyun.com.

AUTHOR CONTRIBUTIONS

ZC: ideas, synthesize study data, original draft, and visualization/data presentation. YZ: oversight and leadership responsibility for the research activity planning and execution. MT, ZY, and ZW: provision of study materials and reagents. BG: review and editing the original draft.

REFERENCES

Balakrishnan, G., Sastikumar, D., Kuppusami, P., Babu, R. V., and Song, J. I. (2018). Microstructural and Mechanical Properties of Al2O3/ZrO2 Nanomultilayer Thin Films Prepared by Pulsed Laser Deposition. *Appl. Phys. A* 124, 158–165. doi:10.1007/s00339-018-1576-7

Cox, B. (2005). Some Thoughts on the Mechanisms of In-Reactor Corrosion of Zirconium Alloys[J]. *J. Nucl. Mater.* 336 (2-3), 331–368. doi:10.1016/j.jnucmat.2004.09.029

Cox, B., and Wu, C. (1995). Transient Effects of Lithium Hydroxide and Boric Acid on Zircaloy Corrosion. *J. Nucl. Mater.* 224, 169–178. doi:10.1016/0022-3115(95)00043-7

Dong, Y., Motta, A. T., and Marquis, E. A. (2013). Atom Probe Tomography Study of Alloying Element Distributions in Zr Alloys and Their Oxides. *J. Nucl. Mater.* 442, 270–281. doi:10.1016/j.jnucmat.2013.08.055

Duan, Z., Yang, H., Satoh, Y., Murakami, K., Kano, S., Zhao, Z., et al. (2017). Current Status of Materials Development of Nuclear Fuel Cladding Tubes for Light Water Reactors. *Nucl. Eng. Des.* 316, 131–150. doi:10.1016/j.nucengdes.2017.02.031

Garzarolli, F., Beck, W., and Fuchs, H. P. (1993). *Recent Occurrences of Abnormal Increased Fuel Rod Corrosion in PWRs: Pro.* Washington DC., USA: EPRI-PWR fuel rod corrosion workshop.

Garzarolli, F., Seidel, H., and Tricot, R. (1991). "Oxide Growth Mechanism on Zirconium Alloys," in Proceedings of 9th International Symposium on zirconium in the nuclear industry, Kobe, Japan, November 5–8, 1990. (ASTM STP).

Gravie, R. C., and Nicholson, P. S. (1972). Phase Anlysis in Zirconia Systems [J]. *J. Am. Ceram. Soc.* 55 (6), 303–305. doi:10.1111/j.1151-2916.1972.tb11290.x

Gravie, R. C., and Nicholson, P. S. (2006). Structure and Thermomechanical Properties of Partially Stabilized Zirconia in CaO-ZrO_2 System[M]. *J. Am. Ceram. Soc.* 55, 259–273. doi:10.1111/j.1151-2916.1972.tb11241.x

Han, J. H., and Rheem, K. S. (1994). The Corrosion Characteristics of Zircaloy-4 Fuel Cladding in LiOH-H3bo3 Solutions. *J. Nucl. Mater.* 217, 197–199. doi:10.1016/0022-3115(94)90321-2

Kim, T.-K., Choi, B.-S., Jeong, Y.-H., Lee, D.-J., and Chang, M.-H. (2002). Effects of Annealing on Tensile Property and Corrosion Behavior of Ti-Al-Zr Alloy. *J. Nucl. Mater.* 301, 81–89. doi:10.1016/s0022-3115(02)00710-9

Kim, T. K., Baek, J. H., Choi, B. K., and Jeong, Y. H. (2007). Influence of Ammonia on the Corrosion Behavior of Ti–Al–Zr Alloy in 360°C Water. *Mater. Mat. Int.* 13 (1), 47–52. doi:10.1007/bf03027822

Krausová, A., Macák, J., and Sajdl, P. (2015). *In-situ* Electrochemical Study of Zr1Nb Alloy Corrosion in High Temperature Li^+ Containing Water[J]. *J. Nucl. Mater.* 467, 302–310. doi:10.1016/j.jnucmat.2015.10.005

Kritskii, V. G., Berezina, I. G., and Motkova, E. A. (2013). Simulating the Corrosion of Zirconium Alloys in the Water Coolant of VVER Reactors. *Therm. Eng.* 60, 457–464. doi:10.1134/s0040601513070057

Kysela, J., Zmítko, M., Yurmanov, V. A., and Tiapkov, V. F. (1996). Primary Coolant Chemistry in VVER Units. *Nucl. Eng. Des.* 160, 185–192. doi:10.1016/0029-5493(95)01096-3

Lai, P., Lu, J., Zhang, H., Liu, Q., Zeng, Q., Guo, X., et al. (2020). The Corrosion Behavior of M5 (Zr-1Nb-0.12O) Alloy in 360 °C Water with Dissolved Oxygen. *J. Nucl. Mater.* 532, 152079. doi:10.1016/j.jnucmat.2020.152079

Liu, J., Yu, H., Karamched, P., Hu, J., He, G., Goran, D., et al. (2019). Mechanism of the α-Zr to Hexagonal-ZrO Transformation and its Impact on the Corrosion Performance of Nuclear Zr Alloys. *Acta Mater.* 179, 328–341. doi:10.1016/j.actamat.2019.08.051

Lustman, B., and Kerze, F. (1955). *The Metallurgy of zirconium[M]*. New York, USA: McGraw-Hill book company inc.

Macdonald, D. D. (2012). Some Personal Adventures in Passivity-A Review of the Point Defect Model for Film Growth. *Russ. J. Electrochem* 48 (3), 235–258. doi:10.1134/s1023193512030068

Malinovschi, V., Martin, A., and Negrea, V. (2017). Tetragonal ZrO_2 Phase Stabilization in Coating Layers Prepared on Zr-2.5%Nb Alloy during Plasma Electrolytic Oxidation in Sodium Aluminate Electrolytes[J]. *Mater. Res. express* 4, 95702. doi:10.1088/2053-1591/aa87c9

Motta, A. T., Couet, A., and Comstock, R. J. (2015). Corrosion of Zirconium Alloys Used for Nuclear Fuel Cladding. *Annu. Rev. Mat. Res.* 45, 311–343. doi:10.1146/annurev-matsci-070214-020951

Ni, N., Hudson, D., Wei, J., Wang, P., Lozano-Perez, S., Smith, G. D. W., et al. (2012). How the Crystallography and Nanoscale Chemistry of the Metal/oxide Interface Develops during the Aqueous Oxidation of Zirconium Cladding Alloys. *Acta Mater.* 60, 7132–7149. doi:10.1016/j.actamat.2012.09.021

Polatidis, E., Frankel, P., Wei, J., Klaus, M., Comstock, R. J., Ambard, A., et al. (2013). Residual Stresses and Tetragonal Phase Fraction Characterisation of Corrosion Tested Zircaloy-4 Using Energy Dispersive Synchrotron X-Ray Diffraction. *J. Nucl. Mater.* 432, 102–112. doi:10.1016/j.jnucmat.2012.07.025

Wei, K. J., Wang, X. P., Zhu, M. H., Chi, X. U., Xue, W., Zhang, J., et al. (2020). Effects of Li, B and H Elements on Corrosion Property of Oxide Films on ZIRLO Alloy in 300 null/14MPa Lithium Borate Buffer Solutions[J]. *Corros. Sci.* 107, 2411–2502. doi:10.1021/acsami.1c06204

Wei, K., Wang, X., and Li, J. (2020). *In-situ* Electrochemical Study of Plasma Electrolytic Oxidation Treated Zr3Al Based Alloy in 300°C/14 MPa Lithium Borate Buffer Solution[J]. *Thin solid films* 707, 138006. doi:10.1016/j.tsf.2020.138066

Xie, S., Zhou, B., Liang, X., Li, Q., Liu, W., Yao, M., et al. (2020). The Distribution of Li Ions in the Oxide Film Formed on Zircaloy-4 Corroded in Lithiated Water at 633 K. *Materials* 13 (4), 873–880. doi:10.3390/ma13040873

Yilmazbayhan, A., Breval, E., Motta, A. T., and Comstock, R. J. (2006). Transmission Electron Microscopy Examination of Oxide Layers Formed on Zr Alloys. *J. Nucl. Mater.* 349 (3), 265–281. doi:10.1016/j.jnucmat.2005.10.012